Nanoscale

RSC Publishing

PAPER

View Article Online
View Journal | View Issue



Cite this: *Nanoscale*, 2013, **5**, 7467

# Enhancing the plasma illumination behaviour of microplasma devices using microcrystalline/ultrananocrystalline hybrid diamond materials as cathodes†

Tinghsun Chang,[a] Shiucheng Lou,[b] Huangchin Chen,[c] Chulung Chen,[b] Chiyoung Lee,[a] Nyanhwa Tai*[a] and Inan Lin*[c]

The properties of capacity-type microplasma devices were significantly enhanced due to the utilisation of hybrid diamond films as cathodes. The performance of the microplasma devices was closely correlated with the electron field emission (EFE) properties of the diamond cathode materials. The nanoemitters, which were prepared by growing duplex-structured diamond films [microcrystalline diamond (MCD)/ultrananocrystalline diamond (UNCD)] on Si-pyramid templates *via* a two-step microwave plasma enhanced chemical vapour deposition (MPE-CVD) process, exhibited improved EFE properties ($E_0$ = 5.99 V $\mu m^{-1}$, $J_e$ = 1.10 mA $cm^{-2}$ at 8.50 V $\mu m^{-1}$ applied field), resulting in superior microplasma device performance (with a lower threshold field of 200 V $mm^{-1}$ and a higher plasma current density of 7.80 mA $cm^{-2}$) in comparison with UNCD film devices prepared using a single-step MPE-CVD process. The superior EFE properties of the duplex-structured MCD–UNCD films relative to those of the UNCD films can be attributed to the unique granular structure of the diamond films. High-resolution transmission electron microscopy reveals that the MCD–UNCD films consisted of abundant graphitic phases located at the periphery of large diamond aggregates and at the boundaries between the ultra-small diamond grains. The presence of the graphite phase is presumed to be the prime factor that renders these films more conductive and causes these films to exhibit higher EFE properties, thus resulting in the improved plasma illumination properties of the microplasma devices.

Received 22nd April 2013
Accepted 13th June 2013

DOI: 10.1039/c3nr01992f

**www.rsc.org/nanoscale**

## 1 Introduction

Microcavity plasma devices exhibit great potential for a broad spectrum of applications in material synthesis, environmental sensing, and elemental analysis because of their favourable power loading (on the order of kW $cm^{-3}$) and their ability to operate continuously at pressures above one atmosphere.[1–5] These devices disclose a new area of photonic technology at the interface of plasma science and optoelectronics.[6–8] The plasma display technology has advanced considerably over the past decade, but challenges remain such as the insufficient luminous efficiency of the plasma devices.[9] The development of a cathode material that can efficiently emit electrons for the purpose of improving the performance of a plasma illumination device is of prime importance. Diamond films, which exhibit intrinsically large secondary electron emission efficiencies ($\gamma$-coefficient), are suitable materials for the microplasma device application.[10] Numerous studies have been performed on the growth, characterisation and applications of single crystalline and microcrystalline diamond (MCD) over the last few decades. Recently, the main focus has been directed towards the synthesis and characterisation of ultrananocrystalline diamond (UNCD) films[11] because of their excellent properties. Several of these properties actually exceed those of conventional diamond materials with micron-sized grains.[12] In addition to their remarkable physical and chemical properties, UNCD films also exhibit superior electron field emission (EFE) properties and can potentially be applied as materials for fabricating electron field emitters.[13–15] The excellent properties are due to the presence of nanosized grains. As the grain size in UNCD films decreases to less than 10 nm, the surface smoothness significantly increases, making it possible to directly fabricate a device.[16] Additionally, the decrease in diamond grain size increases the amount of grain boundaries, which contain non-diamond-type carbon, including $sp^3$ and $sp^2$ carbon materials, as well as hydrocarbons and amorphous carbon. The presence of these species in the film leads to a significant improvement in electrical properties. Moreover, in comparison with MCD

[a]*Department of Materials Science and Engineering, National Tsinghua University, Hsinchu, Taiwan 30013, Republic of China. E-mail: nhtai@mx.nthu.edu.tw; Fax: +886 35737406; Tel: +886 35715131 ext. 42568*

[b]*Department of Photonics Engineering, Yuanze University, Chungli, Taiwan 32003, Republic of China*

[c]*Department of Physics, Tamkang University, Tamsui, Taiwan 25371, Republic of China. E-mail: inanlin@mail.tku.edu.tw; Fax: +886-2-26209917; Tel: +886-2-26268907*

† Electronic supplementary information (ESI) available. See DOI: 10.1039/c3nr01992f

films, the UNCD films exhibit better mechanical stability,[12] and excellent EFE properties have also been reported for UNCD films.[17–19] Among the various potential applications of a diamond electron field emitter, using UNCD as an electron source for microcavity plasma devices appears to be the most promising.

In this study, we utilised Si nanostructures to grow highly conductive diamond films for the purpose of enhancing the plasma illumination properties of the capacitive-type plasma devices (CP-devices). The detailed microstructure of these films was investigated using high resolution transmission electron microscopy (HRTEM) to elucidate the mechanism that generated the enhanced properties of the MCD–UNCD hybrid cathode.

## 2 Experimental

### 2.1 Synthesis of UNCD–Si-pyramid structures

To prepare a high EFE material to serve as a cathode for the microplasma device, a Si-pyramid array was first fabricated, which served as a template for growing the diamond film. A 1.0 μm thick photoresist (PR, EPG512) film was spin coated on a Si substrate, which was then patterned by a conventional photolithographic process to form a square pattern of approximately 6 μm × 6 μm in size with 10 μm separations (step 1, Fig. 1). The Si substrate containing the PR pattern was then subjected to reactive ion etching using $CF_4$ + $SF_6$, followed by stripping of the PR using the Ar plasma to form Si templates consisting of a Si-pyramid array (steps 2 and 3, Fig. 1). Some of the Si templates were sputtered using a thin layer of Au (100 nm) (step 4, Fig. 1). A 10 nm Cr layer was coated on top of the Si templates prior to introducing the Au-interlayer to enhance the adhesion between the Au-interlayer and the Si templates. The Si templates, with or without the Au-interlayer, were then ultrasonicated in a methanol solution containing nanodiamond particles (~100 nm) and nano-Ti powder (<40 mesh). The UNCD films were then grown on these Si templates (step 5, Fig. 1) using the microwave plasma enhanced chemical vapour deposition (MPE-CVD) process. During the growth of UNCD films, the plasma ($CH_4$/Ar = 1/99 sccm) was excited using a microwave (2.45 GHz) source with 1200 W under 120 Torr of total pressure. The UNCD films with a typical thickness of 300 nm were grown without external heating. The substrate temperature was estimated to be approximately 475 °C using a thermocouple embedded in the stainless steel substrate holder. The samples that did not contain the Au-interlayer were designated as $UNCD_{Si\text{-}pyramid}$, whereas those containing this layer were designated as $UNCD_{Au/Si\text{-}pyramid}$.

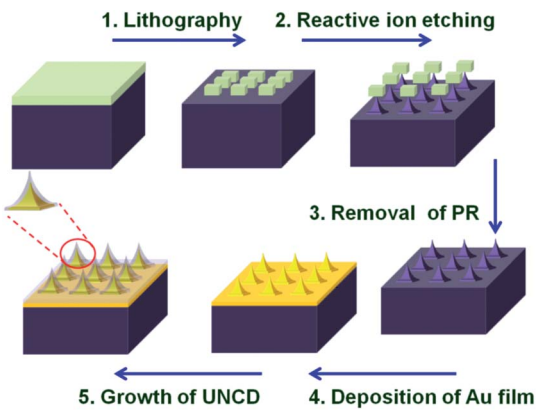


**Fig. 1** The schematics of the fabrication process of Si-pyramid array templates for growing the diamond films: (1) patterning of photoresist by an optical lithography process, (2) reactive ion etching for forming the Si pyramid, (3) removal of the photoresist, (4) deposition of the Au-interlayer (if necessary) and (5) growth of diamond films. After step 5, some samples were subjected to the two-step MPE-CVD process for growing the MCD.

### 2.2 Morphological and structural characterization

The morphologies of the as-prepared and UNCD coated Si templates were examined using field emission scanning electron microscopy (FESEM; JEOL JSM-6500F). The bonding structure of the UNCD films coated on Si templates was investigated using 514 nm Raman spectroscopy (Lab Raman HR800, Jobin Yvon). Microstructure characterisation of the UNCD films coated on Si templates was studied by HRTEM (JEOL-2100F).

### 2.3 EFE measurements

The EFE properties of the UNCD-coated Si templates were measured using a parallel plate set-up in which the anode (tungsten rod, 1.0 mm in diameter) was separated from the cathode (UNCD-coated Si templates) and the cathode-to-anode distance was controlled using an adjustable micrometer attached to the anode. The current-to-voltage properties of the UNCD coated Si templates were measured using a Keithley 237 electron source meter operating in a high-vacuum environment (<$5 \times 10^{-6}$ Torr). Curves of current density *versus* applied field (*J*–*E*) were modelled using the Fowler–Nordheim (F–N) formula.[20] The turn-on field for inducing the EFE process was calculated from the intersection of two lines extrapolated from the low-field and high-field segments of the F–N plots, which were plotted as $J/E^2$ *versus* $1/E$ curves.

### 2.4 Plasma illumination measurements

The plasma illumination characteristics, including the change in plasma images as a function of applied voltage for a CP-device, were characterised using a parallel plate apparatus in which the indium tin oxide (ITO) coated glass plates (the anode) were separated from the UNCD-coated Si templates (the cathode) with a Teflon spacer (1.0 mm in thickness). A cylindrical cavity with a size of approximately 8 mm was formed by drilling a hole in the Teflon spacer. The Ar plasma was excited between the ITO- and UNCD-coated Si templates by applying a positive pulsed voltage (20 000 pulses per s, 0–400 V) to the anode in the Ar environment of ~100 Torr. The current density *versus* applied field for this apparatus was measured using a Keithley 2410 current source electrometer.

## 3 Results and discussion

### 3.1 The characteristics of UNCD films grown on Si-pyramidal arrays

Fig. 1 shows the processes for the preparation of Si nanostructured patterns and the growth of UNCD films. The mask

 

array was defined on the Si substrates using a conventional photolithographic process. The PR patterns can further be utilised as effective masks in fabricating high-quality Si nanostructures *via* RIE to form a Si-pyramid array. The UNCD films were then grown on these Si pyramids, with or without the Au-interlayer, using the MPE-CVD process.

Fig. 2a shows the FESEM micrograph of the Si templates, which reveals that the Si-pyramid arrays are very uniformly fabricated. The tip of the pyramid is approximately 4 μm in size (3.5 μm in height) and is separated from other pyramids by approximately 10 μm. The radius of the tip is approximately 30 nm, as calculated from the FESEM image (the inset of Fig. 2a). Fig. 2b and c show the FESEM morphologies of the $UNCD_{Si\text{-}pyramid}$ and the $UNCD_{Au/Si\text{-}pyramid}$ arrays, respectively. The UNCD films were conformably coated on the Si-pyramid arrays, in both the presence and the absence of the Au-interlayer (insets of Fig. 2b and c). The Si-pyramids are strong enough to survive the ultrasonication seeding process; thus the sharp pyramids can be retained before and after UNCD growth. Such a phenomenon reveals the advantage of using Si-pyramid arrays as templates over the use of Si nanowires (SiNWs) prepared by the self-galvanic etching process.[21,22] Although the SiNWs were extremely sharp with a high aspect ratio (typically 30 nm in diameter and 100 μm in length), they were very fragile and could not survive the ultrasonication seeding process. Not only the SiNWs were seriously damaged, but the UNCD films grown on these SiNWs often formed in bundles, which were too close to one another that resulted in a significant electric field screening effect. Accordingly, UNCD–SiNWs nanoemitters exhibited inferior EFE properties.[21] The UNCD grown on Si-pyramids not only retained the same sharpness as the as-prepared Si templates, but the separation between the tips was large enough to circumvent the electric field screening effect. Therefore, improved EFE properties were expected for the $UNCD_{Si\text{-}pyramid}$ (or $UNCD_{Au/Si\text{-}pyramid}$) array emitters.

Fig. 3a and b show the SEM morphologies of the UNCD films coated on the planar regions located in between the Si-pyramid tip. These figures demonstrate that the surface of the UNCD films is smooth. The TEM micrograph, shown as an inset in Fig. 3a, suggests that the UNCD films contain ultra-small diamond grains (~5 nm in size) with a very uniform size distribution. Fig. 4a shows the Raman spectroscopic data of the UNCD films, revealing that both $UNCD_{Si\text{-}pyramid}$ and $UNCD_{Au/Si\text{-}pyramid}$ films contain large diffuse Raman resonance peaks, which are characteristic of diamond films with ultra-small grain granular structure.[23–26] The Raman spectrum of the $UNCD_{Si\text{-}pyramid}$ film (curve "i", Fig. 4a) contains $\nu_1$ and $\nu_3$ bands at 1120 $cm^{-1}$ and 1480 $cm^{-1}$, respectively, which correspond to the *trans*-polyacetylene phase located at the grain boundaries of the UNCD films.[25,26] In addition, the D*- and G-bands at 1350 $cm^{-1}$ and 1580 $cm^{-1}$, respectively, correspond to the disordered carbon and graphitic phase.[23,24] Curve "ii" in Fig. 4a shows that the Raman spectrum of $UNCD_{Au/Si\text{-}pyramid}$ films is similar to that of the $UNCD_{Si\text{-}pyramid}$ films because they also contain diffuse $\nu_1$-, $\nu_3$-, D*- and G-band resonance peaks. It should be noted that the D-band resonance peak at 1332 $cm^{-1}$, which corresponds to the $\Gamma_{2g}$ mode of the diamond lattice, is not observed in these UNCD films.

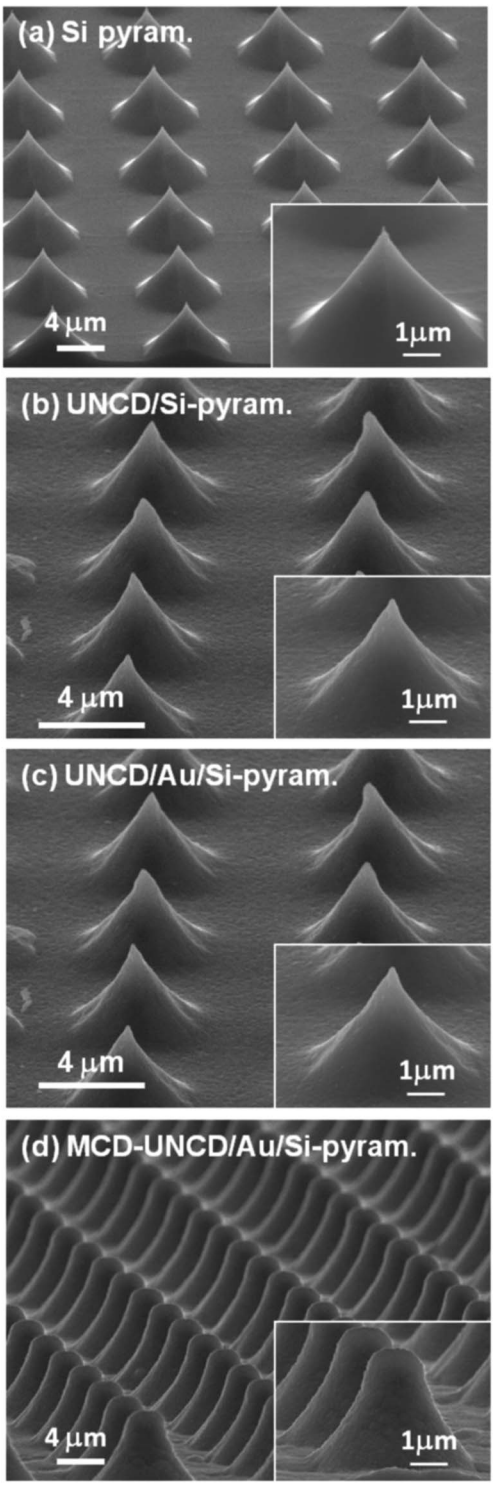


**Fig. 2** SEM micrographs of (a) the as-prepared Si-pyramid arrays, (b) the $UNCD_{Si\text{-}pyramid}$ that was grown directly on the Si-pyramid arrays without the Au-interlayer, (c) the $UNCD_{Au/Si\text{-}pyramid}$ that was grown on the Si-pyramid arrays with an Au-interlayer (100 nm) and (d) the MCD–$UNCD_{Au/Si\text{-}pyramid}$ grown using the two-step MPE-CVD process on Si-pyramid arrays with an Au-interlayer (100 nm).

The use of the Au-interlayer does not appear to significantly alter the FESEM morphology or the Raman bonding characteristics of the UNCD films. However, it does considerably enhance

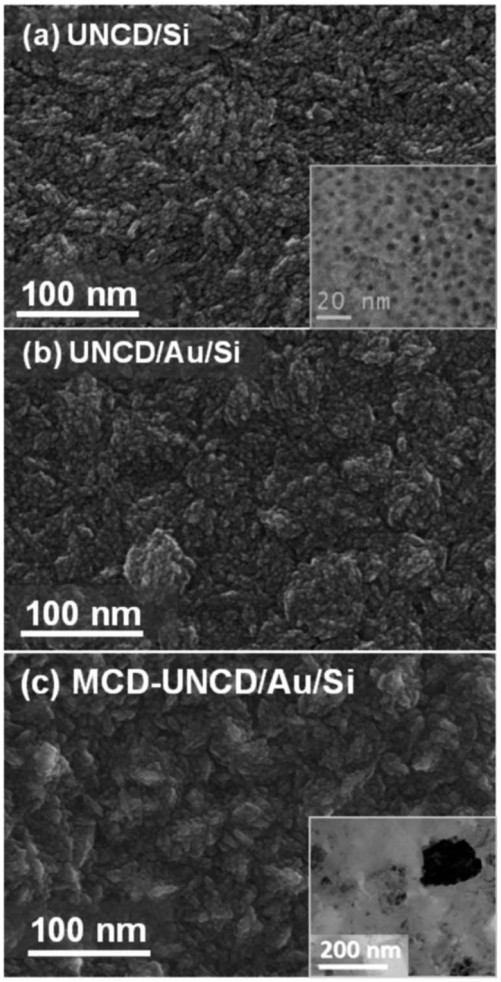


**Fig. 3** (a and b) SEM micrographs of planar UNCD films grown on the planar Si substrates, which were located at the base of the Si templates in the absence (a) and presence (b) of an Au-interlayer. (c) Planar MCD–UNCD grown on planar Si substrates using the two-step MPE-CVD process with an Au-interlayer (100 nm). The insets in "a" and "c" are the corresponding HRTEM micrographs.

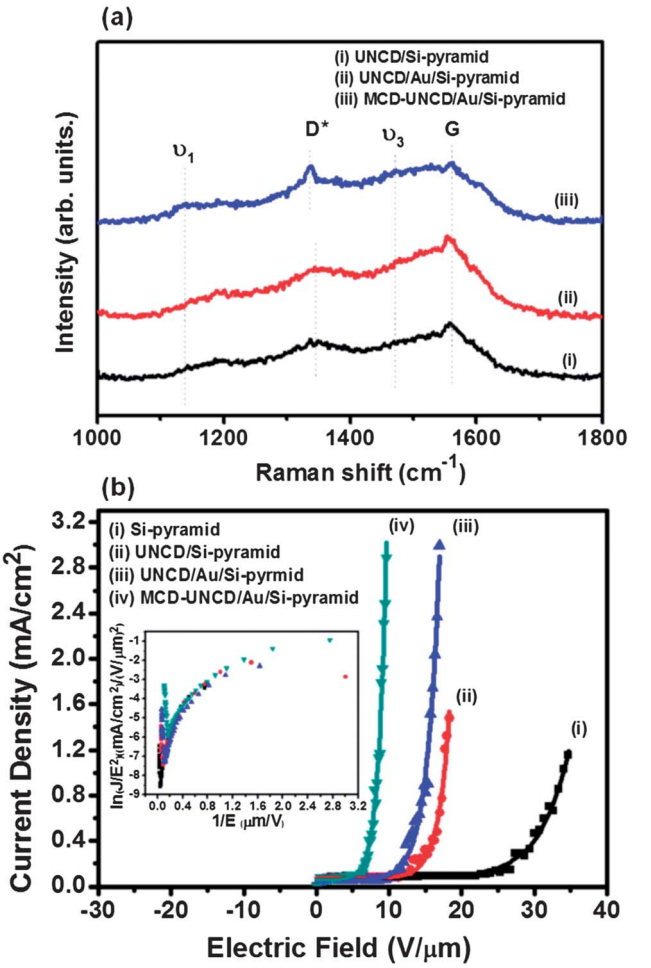


**Fig. 4** (a) The Raman spectroscopy and (b) EFE properties of (i) the Si-pyramid, (ii) the $UNCD_{Si\text{-}pyramid}$, (iii) the $UNCD_{Au/Si\text{-}pyramid}$ and (iv) the MCD–$UNCD_{Au/Si\text{-}pyramid}$ nanoemitters.

the EFE properties of the UNCD-based nanoemitters. Fig. 4b shows that the $UNCD_{Si\text{-}pyramid}$ nanoemitters could be turned on at $(E_0)_{UNCD/Si\text{-}pyramid} = 11.70$ V μm$^{-1}$ and attained an EFE current density of $(J_e)_{UNCD/Si\text{-}pyramid} = 1.60$ mA cm$^{-2}$ at an applied field of 18.50 V μm$^{-1}$ (curve "ii"), whereas the $UNCD_{Au/Si\text{-}pyramid}$ nanoemitters merely needed a lower field of $(E_0)_{UNCD/Au/Si\text{-}pyramid} = 9.23$ V μm$^{-1}$ to turn on the EFE process and achieved a higher EFE capacity, $(J_e)_{UNCD/Au/Si\text{-}pyramid} = 2.90$ mA cm$^{-2}$ at an applied field of 17.0 V μm$^{-1}$ (curve "iii"). In contrast, we observed negligible field emission from bare Si pyramid arrays with a turn-on field of 23.40 V μm$^{-1}$ and a low EFE current density of 0.078 mA cm$^{-2}$ at an applied field of 18.50 V μm$^{-1}$ (curve "i"). The benefit of using Au as an interlayer for enhancing the electric properties of the UNCD nanoemitters becomes more apparent when comparing the plasma illumination behaviour of microplasma devices prepared using these nanoemitters as cathodes. Fig. 5a–c show a series of the plasma images obtained with an increasing applied voltage. The devices that employ $UNCD_{Si\text{-}pyramid}$ (or $UNCD_{Au/Si\text{-}pyramid}$) nanostructures as the cathode (Fig. 5b and c) exhibit superior plasma illumination behaviour to those obtained using Si-pyramid arrays as the cathode (Fig. 5a). The former devices (Fig. 5b) can be ignited at a low voltage of 210 V, which corresponds to a threshold field of $(E_{th})_{pl.} = 210$ V mm$^{-1}$. The plasma current density, which is proportional to the ion (or electron) density on the plasma, increases gradually with applied voltage and reaches a maximum value of $(J_{pl.})_{UNCD/Si\text{-}pyramid} = 5.90$ mA cm$^{-2}$ at an applied field of 350 V mm$^{-1}$ (curve "ii", Fig. 6a). Furthermore, the microplasma devices obtained using $UNCD_{Au/Si\text{-}pyramid}$ nanoemitters as the cathode can attain an even higher plasma current density of $(J_{pl.})_{UNCD/Au/Si\text{-}pyramid} = 6.20$ mA cm$^{-2}$ at an applied field of 350 V mm$^{-1}$ (curve "iii", Fig. 6a), although the threshold field for plasma ignition is the same (210 V mm$^{-1}$). It seems that the smaller turn-on field ($E_0$) in the EFE process does not help lower the threshold field to ignite the plasma illumination process, but instead leads to a higher EFE current density with increasing plasma density. This phenomenon will be further discussed later. The EFE and plasma illumination properties of these samples are summarised in Table 1.

The superior EFE properties of the $UNCD_{Au/Si\text{-}pyramid}$ nanoemitters and the improved plasma illumination behaviour of

 

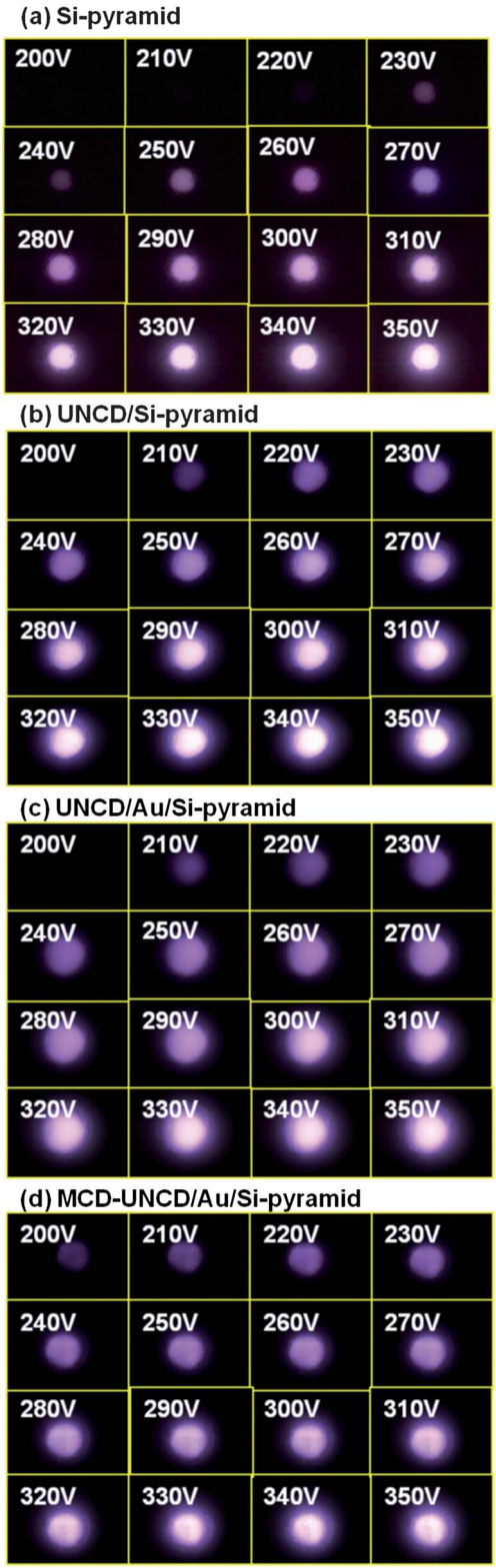


**Fig. 5** Plasma illumination behaviour as demonstrated by plasma images obtained under an applied voltage for microplasma devices prepared using the following cathode materials: (a) Si-pyramid, (b) $UNCD_{Si\text{-}pyramid}$, (c) $UNCD_{Au/Si\text{-}pyramid}$ and (d) MCD–$UNCD_{Au/Si\text{-}pyramid}$.

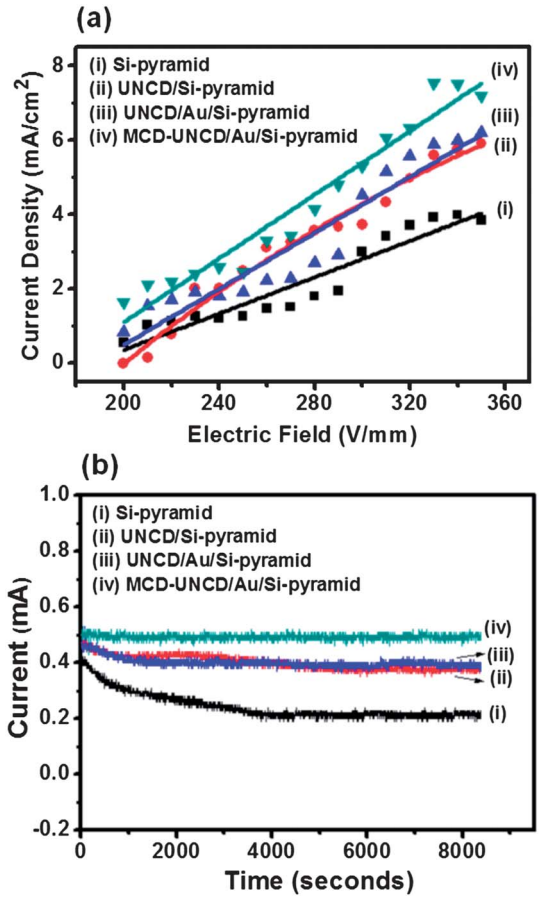


**Fig. 6** (a) The plasma current density as a function of applied field for microplasma devices, as well as (b) the plasma current stability tested for more than 2 hours, using the following cathode materials: (i) Si-pyramid, (ii) $UNCD_{Si\text{-}pyramid}$, (iii) $UNCD_{Au/Si\text{-}pyramid}$, and (iv) MCD–$UNCD_{Au/Si\text{-}pyramid}$.

the corresponding microplasma devices, compared with those of the $UNCD_{Si\text{-}pyramid}$ nanoemitters, are due to the better conductivity of the $UNCD_{Au/Si\text{-}pyramid}$ films. The Hall measurements performed in the van der Pauw configuration (ECOPIA HMS-3000) indicate that the $UNCD_{Au/Si\text{-}pyramid}$ films exhibit good electric conductivity, $\sigma_{UNCD/Au/Si\text{-}pyramid} = 0.78\ (\Omega\ cm)^{-1}$, whereas the $UNCD_{Si\text{-}pyramid}$ films are too resistive to be measurable by this technique. The higher conductivity of the $UNCD_{Au/Si\text{-}pyramid}$ films can be attributed to the improved UNCD–Si interface.

To understand how the Au interlayer modifies the interfacial electrical properties of the UNCD films, we examined the cross-sectional microstructure of the films using TEM. Fig. 7a shows typical cross-sectional TEM micrographs [with the inset showing the corresponding selective area electron diffraction (SAED)] of the UNCD–Si films, revealing that the UNCD–Si interface is straight and neat. However, a more detailed examination using HRTEM reveals a thin, continuous and uniform interfacial layer of a few nanometres in thickness (indicated by an arrow in Fig. 7c). The Fourier-transformed diffractogram images $FT_1$ and $FT_2$ corresponding to areas 1 and 2 in Fig. 7c indicate that the interfacial layer contains amorphous carbon

**Table 1** EFE properties of UNCD films grown on planar Si substrates and the Si-pyramid array templates

| | Conductivity $(\Omega\ cm)^{-1}$ | Electron field emission | | Plasma illumination | |
|---|---|---|---|---|---|
| | | $E_0$[a] (V μm$^{-1}$) | $J_e$[b] (mA cm$^{-2}$) | $(E_{th})_{pl.}$[c] (V mm$^{-1}$) | $J_{pl.}$[d] (mA cm$^{-2}$) |
| Si-pyramids | — | 23.40 | ≤0.01 | 230 | 4.00 |
| $UNCD_{Si\text{-}pyramids}$ | — | 11.70 | 0.04 | 210 | 5.90 |
| $UNCD_{Au/Si\text{-}pyramids}$ | 0.78 | 9.23 | 0.05 | 210 | 6.20 |
| $MCD\text{–}UNCD_{Au/Si\text{-}pyramids}$ | 24.0 | 5.99 | 1.10 | 200 | 7.80 |

[a] $E_0$: the turn-on field derived from Fowler–Nordheim plots, as the intersections of straight lines extrapolated from the low-field and high-field segments of the F–N plots. [b] $J_e$: the electron field emission current density achieved at an applied field of $E_a = 8.50$ V μm$^{-1}$. [c] $E_{th}$: the threshold field for triggering the plasma in the CP-devices. [d] $J_{pl.}$: the plasma current density achieved in the CP-devices at an applied field of $E_{pl.} = 350$ V mm$^{-1}$.

(a-C) and Si, respectively. The FT image corresponding to the entire structure image is shown as $FT_{0c}$, revealing that the region contains UNCD, Si and a-C. In contrast, Fig. 7b shows that for UNCD/Au/Si films there is an interfacial layer of approximately tens of nanometres in thickness located between the UNCD and the Au coating. A Cr layer was not observed, most likely due to the pronounced interdiffusion between the Si substrates and the Au coating. The HRTEM micrograph shown in Fig. 7d indicates that the interfacial layer is a mixture of a-C clusters and SiC clusters. The FT images, $FT_3$ and $FT_4$, in Fig. 7d highlight SiC and a-C clusters marked by dot-square areas 3 and 4, respectively. A continuous a-C layer was not observed in these films. Again, the $FT_{0d}$ in Fig. 7d represents the FT image corresponding to the entire structure image, indicating that the region contains UNCD, SiC and a-C. To illustrate more clearly the distribution of phases in the film, we acquired dark-field images for different phases and then superimposed them to produce composed dark-field (c-DF) images, which are shown in the ESI as Fig. S1a and b.†

### 3.2 The characteristics of the MCD–UNCD films grown on Si-pyramid arrays

The aforementioned observations strongly suggest that enhancing the EFE properties of the cathode materials leads to an improvement in the microplasma device performance. Apparently, increasing the conductivity of the UNCD films is necessary for this purpose. It should be noted that although the UNCD films exhibit better conductivity and superior EFE properties compared with other types of diamond films, there is still room for improvement. The high conductivity and the superb EFE properties of the UNCD films are due to the unique granular structure of the materials. The UNCD films prepared by the conventional one-step MPE-CVD process using $CH_4$/Ar plasma usually contain ultra-small diamond grains (~5 nm in size), which are very uniform in their size distributions and are separated by grain boundaries of considerable thickness (~0.5 to 1.0 Å).[11,12] The grain boundary phases of the UNCD films transport electrons more efficiently than those of the conventional microcrystalline diamond films with large grain size, resulting in significantly better conductivity and EFE properties of the UNCD films. However, the amorphous nature of the grain boundary phase of the UNCD films limits their conductivity. To further improve the EFE properties of the UNCD films, we used a two-step MPE-CVD process to modify the granular structure of the UNCD films. During this process, the Au-coated Si tip templates were first coated with a thin layer of UNCD films using $CH_4/Ar = 1/99$ sccm plasma excited by a 1200 W microwave at 120 Torr for 1 h. This step resulted in a thickness of approximately 300 nm, which served as a seeding layer for a second MPE-CVD treatment performed using a $CH_4/Ar/H_2 = 1/49/50$ sccm plasma and excited by a 1300 W microwave at 80 Torr for 1 h. The total thickness is approximately 800 nm. These diamond films were designated as $MCD\text{–}UNCD_{Au/Si\text{-}pyramid}$ films.

Fig. 2d shows the FESEM morphology of the $MCD\text{–}UNCD_{Au/Si\text{-}pyramid}$ film. The magnified FESEM image (the inset of Fig. 2d) shows the conformably coated MCD–UNCD species on top of the Si-pyramid templates. This two-step MPE-CVD process results in considerable thickening of the Si tips. Fig. 3c shows that the MCD–UNCD films are also very smooth, but the HRTEM micrograph shown in the inset reveals that the granular structure of the films was significantly modified as a result of the two-step MPE-CVD process. There are large diamond aggregates of hundreds of nanometres in size dispersed in a matrix of ultra-small diamond grains. Raman spectroscopy of these $MCD\text{–}UNCD_{Au/Si\text{-}pyramid}$ nanoemitters is provided as curve "iii" in Fig. 4a, indicating that the $MCD\text{–}UNCD_{Au/Si\text{-}pyramid}$ films also contain broad $\nu_1$-, $\nu_3$-, D*- and G-band peaks, which represent diamond with ultra-small grains with a large proportion of grain boundary phases. However, a detailed investigation indicates that the Raman spectrum of the $MCD\text{–}UNCD_{Au/Si\text{-}pyramid}$ films contains a small sharp Raman peak near 1332 cm$^{-1}$ (D-band), which corresponds to the $\Gamma_{2g}$ band of large diamond grains. These observations indicate that the $MCD\text{–}UNCD_{Au/Si\text{-}pyramid}$ films contain some large diamond grains that co-exist with the ultra-small grains, *i.e.*, these films are of a duplex-granular structure. This observation is in agreement with the HRTEM investigation (*cf.* inset, Fig. 3c). The effect of this duplex granular structure on the electrical properties of the films was investigated further in the subsequent section.

Curve "iv" in Fig. 4b shows that the $MCD\text{–}UNCD_{Au/Si\text{-}pyramid}$ nanoemitters exhibit remarkably superior EFE properties compared with those of the $UNCD_{Si\text{-}pyramid}$ (or $UNCD_{Au/Si\text{-}pyramid}$) films. The EFE process of the $MCD\text{–}UNCD_{Au/Si\text{-}pyramid}$

 

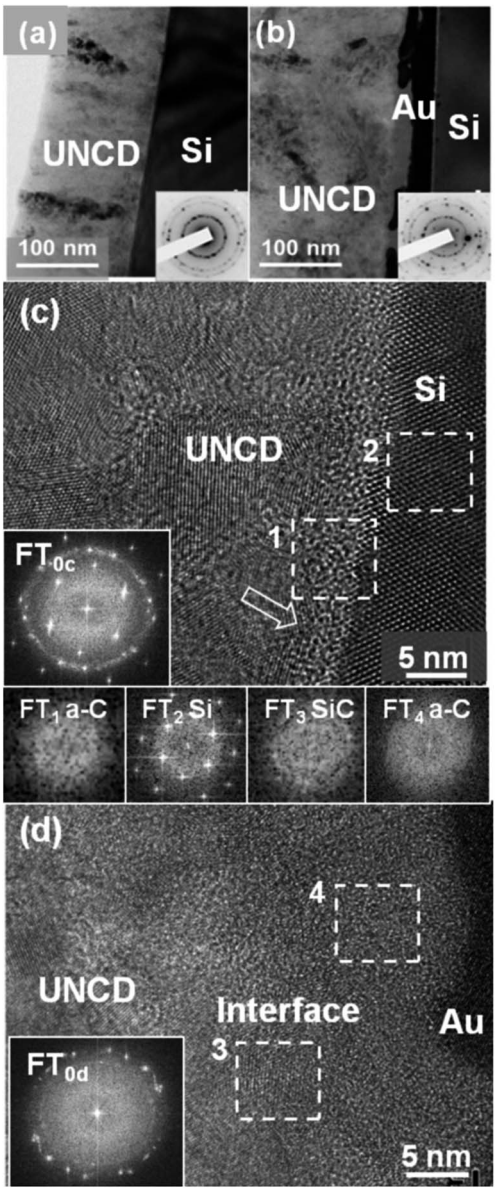


**Fig. 7** BF-TEM images of UNCD films grown on Si in the absence (a) and presence (b) of an Au interlayer. HRTEM images in (c) and (d) show a typical UNCD–Si interface in the absence (c) and presence (d) of an Au interlayer. The insets $FT_{0c}$ and $FT_{0d}$ in (c) and (d) are the Fourier-transformed diffractograms corresponding to the entire structure image of the films in "c" and "d", respectively, whereas $FT_1$ to $FT_4$ are FT images corresponding to areas 1 to 4, respectively.

nanoemitters can be turned on at a considerably lower field of $(E_0)_{MCD–UNCD/Si\text{-}pyramid} = 5.99\ V\ \mu m^{-1}$, attaining a much higher EFE current density of $(J_e)_{MCD–UNCD/Si\text{-}pyramid} = 1.10\ mA\ cm^{-2}$ at an applied field of 8.50 V $\mu m^{-1}$. It should be noted that both $UNCD_{Si\text{-}pyramid}$ and $UNCD_{Au/Si\text{-}pyramid}$ nanoemitters can only emit a low EFE current density of approximately 0.04–0.05 mA $cm^{-2}$ at such a low applied field. Moreover, the microplasma devices using such a high EFE nanoemitter as the cathode can be ignited at a lower threshold field of $(E_{th})_{pl.} = 200\ V\ mm^{-1}$ (Fig. 5d), which produces a higher plasma current density of $(J_{pl.})_{MCD–UNCD/Au/Si\text{-}pyramid} = 7.80\ mA\ cm^{-2}$ at 350 V $mm^{-1}$ (curve "iv", Fig. 6a). Again, the use of high EFE materials, such as $MCD–UNCD_{Au/Si\text{-}pyramid}$ nanoemitters, as cathode materials does not significantly lower the threshold field for igniting the plasma, but enhances the plasma density of the microplasma devices (Table 1). The plasma illumination from $MCD–UNCD_{Au/Si\text{-}pyramid}$ nanoemitters was more stable compared with other nanoemitters. Fig. 6b shows that the plasma current (0.5 mA) of $MCD–UNCD_{Au/Si\text{-}pyramid}$ (curve iv) essentially remains unchanged over two hours of operation, whereas that of the $UNCD_{Au/Si\text{-}pyramid}$ (or $UNCD_{Si\text{-}pyramid}$) devices slightly decreased during the operation, although less significantly than the bare Si-pyramid (curve i). The $MCD–UNCD_{Au/Si\text{-}pyramid}$ nanoemitters exhibit higher life-time stabilities relative to those of the $UNCD_{Au/Si\text{-}pyramid}$ films and the bare Si-pyramid.

It should be noted that the threshold electric field $(E_{th})_{pl.}$ required to trigger the Ar plasma is perceptibly lower than the $E_0$ for inducing the EFE process for the corresponding diamond films. Although the $MCD–UNCD_{Au/Si\text{-}pyramid}$ nanoemitters exhibit a much lower $E_0$ for the EFE process compared with that of the $UNCD_{Au/Si\text{-}pyramid}$ nanoemitters, the threshold field $(E_{th})$ for triggering the illumination process does not reveal a significant difference when the cathode material is changed from the $UNCD_{Au/Si\text{-}pyramid}$ to the $MCD–UNCD_{Au/Si\text{-}pyramid}$ nanoemitters. Such a phenomenon is due to the difference in the mechanism for plasma ignition in an Ar environment (100 Torr) compared to that of the EFE tunnelling process in a high vacuum environment ($10^{-6}$ Torr). Under the former conditions, the plasma can be triggered when the electrons emitted from the cathode attain sufficient kinetic energy to ionise the gas molecules (*e.g.*, 15.7 eV for Ar species).[27] In this voltage regime, the electric field imposed on the cathode materials is far below the $E_0$ needed for inducing a significant amount of EFE current, but the abundant secondary electrons induced by the $Ar^+$ ion bombardment are sufficient to trigger an ionisation cascade of Ar gas molecules, inducing the onset of plasma. Therefore, it appears that the low turn-on field for the $MCD–UNCD_{Au/Si\text{-}pyramid}$ is not helpful in lowering the threshold field for plasma ignition. However, a high plasma illumination current density was observed when the $MCD–UNCD_{Au/Si\text{-}pyramid}$ film was used as a cathode. This phenomenon indicates that when the plasma is ignited, the electric field experienced by the cathode materials is large enough to induce the EFE process in the materials. However, more detailed investigations are necessary to elucidate the correlation between the EFE and the plasma illumination processes.

Furthermore, the improved EFE properties of the $MCD–UNCD_{Au/Si\text{-}pyramid}$ nanoemitters that led to the enhanced plasma illumination behaviour of the microplasma devices are due to the improved conductivity of the films. The Hall measurements obtained using van der Pauw configuration show that the $MCD–UNCD_{Au/Si\text{-}pyramid}$ films exhibit an electric conductivity $(\sigma)$ as high as 24.0 $(\Omega\ cm)^{-1}$, which is superior to those of the $UNCD_{Au/Si\text{-}pyramid}$ and $UNCD_{Si\text{-}pyramid}$ films. Questions remain about how the two-step MPE-CVD process results in improved conductivity of the MCD–UNCD. To elucidate the mechanism that led to an improvement in the electrical properties, the microstructure of the MCD–UNCD films was investigated by HRTEM.

It should be noted that the UNCD nucleation layer contained randomly oriented small diamond grains with a spherical

geometry (approximately 5 nm in diameter) and a uniform size distribution. The granular structure of the UNCD nucleation layer was significantly modified due to the secondary MPE-CVD process. Fig. 8a shows the bright field TEM (BF-TEM) image of the MCD–UNCD films, revealing the presence of large diamond aggregates of approximately hundreds of nanometers in size that are evenly dispersed in a small-grain matrix. The SAED pattern (inset, Fig. 8a) shows that there are ring-shaped diffraction patterns together with the discrete diffraction spots, indicating the coexistence of small diamond grains and large diamond aggregates, which is in accordance with the Raman data (*cf.* Fig. 4a). The c-DF images clearly illustrate the distribution of phases in the films corresponding to Fig. 8a (see Fig. S2a in the ESI for details†). Fig. 8c shows the HRTEM image of a typical region near the periphery of large diamond aggregates (marked in Fig. 8a), indicating that the diamond grains contain a large proportion of planar defects. There are areas containing parallel fringes of irregular spacing, which correspond to stacking faults,[28] and other areas containing parallel fringes of regular spacing, which correspond to the hexagonal diamond phase.[28] The FT image ($FT_{0c}$) corresponding to the entire structure image indicates the presence of a diffuse ring in the centre of the $FT_{0c}$ image, in addition to the diamond diffraction pattern. Intriguingly, images $FT_1$ and $FT_2$ corresponding to areas 1 and 2 show that the periphery region of the MCD–UNCD film contains a graphitic phase surrounding the diamond aggregates. These observations suggest a coalescence process induced by the presence of a graphite phase, which is accompanied by the formation of large aggregates.

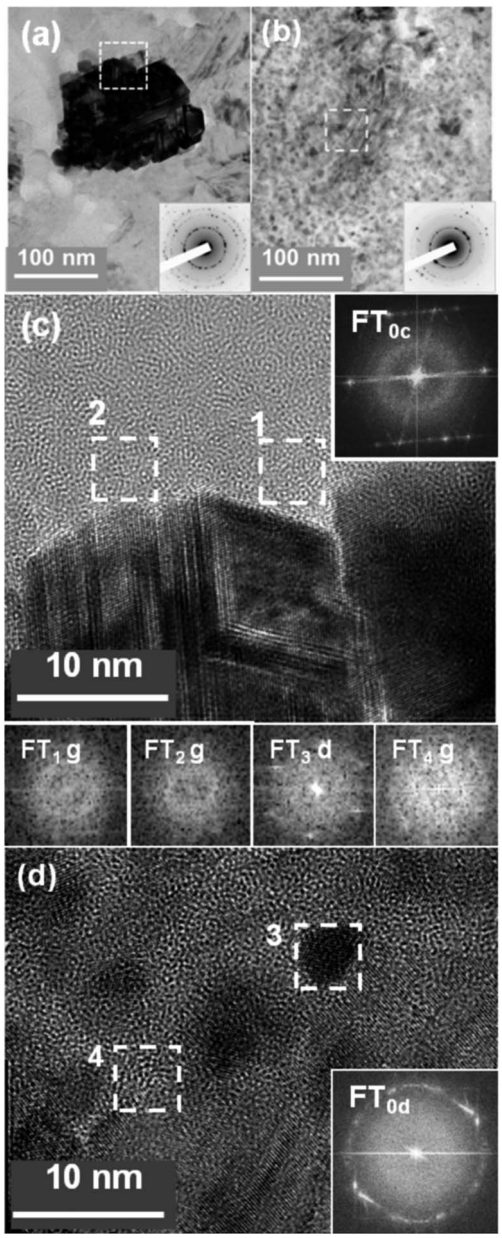


**Fig. 8** (a) The BF-TEM image of the MCD–$UNCD_{Au/Si}$ films grown on the Si-pyramid using the Au interlayer and (b) those of tilted samples, such that the large diamond aggregates are away from the zone-axis, revealing a granular structure other that the aggregates. The HRTEM structure images (c) and (d) correspond to regions marked in "a" and "b", respectively. The $FT_{0c}$ and $FT_{0d}$ images show the FT diffractograms corresponding to the entire structure images "c" and "d", respectively, whereas the $FT_1$ to $FT_4$ images correspond to areas 1 to 4, respectively.

Furthermore, the MCD–UNCD samples were tilted to examine phases other than the large diamond aggregates discussed above. Fig. 8b shows the BF-TEM image of the same region as that in Fig. 8a, after the samples were tilted such that the aggregates are away from the zone axis, revealing that there are large proportions of nanometre-sized diamond grains distributed in the same region. The c-DF image in Fig. S2b† more clearly illustrates the distribution of phases in this same region. Clearly, the large diamond aggregates are formed by the coalescence of ultra-small diamond grains present in the UNCD nucleation layer during the secondary MPE-CVD process. The more detailed granular structure of the region designated in Fig. 8b is shown as the HRTEM structure image in Fig. 8d. This figure reveals that this region contains some small spherical grains, which are approximately 5–8 nm in size and are separated by grain boundaries of considerable thickness. The FT image ($FT_{0d}$) corresponding to the entire structure image indicates the presence of a diffuse ring in the centre of the $FT_{0d}$ image, in addition to the ring-shaped diamond diffraction pattern. This $FT_{0d}$ image again suggests the presence of a graphitic phase (or a-C) in the small-grain region. The typical diamond grains and graphitic clusters are highlighted by the FT images, $FT_3$ and $FT_4$, corresponding to areas 3 and 4, respectively.

To reiterate, the HRTEM analysis reveals that, while the UNCD films contain ultra-small and randomly oriented diamond grains, the MCD–UNCD films grown on the UNCD layer exhibit a duplex granular structure, with numerous large diamond aggregates evenly distributed inside the small-grain matrix. The complicated defect structure contained in the large aggregates of the MCD–UNCD films (*cf.* Fig. 8c) reveals that the aggregates were formed *via* the coalescence of nanodiamonds rather than through the lateral growth of a diamond seed. However, the presence of large aggregates does not appear to enhance the EFE properties of the MCD–UNCD films, as they contain very few grain boundaries for transporting electrons. Presumably, the prime factor that significantly improved the electron transport and enhanced the EFE properties of the MCD–UNCD cathode materials is the formation of a graphite

 

phase around the periphery of large aggregates and along the grain boundaries in the small-grain regions, resulting in the formation of interconnected paths.[29] Accordingly, this factor also enhanced the plasma illumination properties of the microplasma devices.

## 4 Conclusions

The effect of the cathode materials on the plasma illumination properties of the CP-devices was examined systematically in this study. The plasma illumination characteristics of CP-devices are closely correlated with the EFE behaviour of the cathode materials. MCD–$UNCD_{Au/Si\text{-}pyramid}$ nanoemitters, which were grown *via* a two-step MPE-CVD process, exhibited superior electric conductivity ($\sigma_{MCD\text{–}UNCD} = 24.0\ (\Omega\ cm)^{-1}$) compared with the $UNCD_{Au/Si\text{-}pyramid}$ devices ($\sigma_{UNCD} = 0.78\ (\Omega\ cm)^{-1}$), which were grown using a one-step MPE-CVD process in $CH_4$/Ar plasma. The EFE process of the former materials can be turned on at $(E_0)_{MCD\text{–}UNCD/Au/Si\text{-}pyramid} = 5.99\ V\ \mu m^{-1}$, achieving a higher EFE current density of $(J_e)_{MCD\text{–}UNCD/Au/Si\text{-}pyramid} = 1.10\ mA\ cm^{-2}$ at an applied field of $8.50\ V\ \mu m^{-1}$, whereas that of the latter materials required $(E_0)_{UNCD/Au/Si\text{-}pyramid} = 9.23\ V\ \mu m^{-1}$ to turn on the EFE process and produced only $(J_e)_{UNCD/Au/Si\text{-}pyramid} = 0.05\ mA\ cm^{-2}$ at the same applied field. While the plasma illumination process can be triggered at nearly the same threshold field of approximately 200–210 V $mm^{-1}$ regardless of the characteristics of the cathode materials, the plasma illumination intensity and plasma current density were higher when materials with better EFE properties were used as cathodes. The plasma illumination current density was approximately $(J_{pl.})_{MCD\text{–}UNCD} = 7.80\ mA\ cm^{-2}$ (at an applied field of 350 V $mm^{-1}$) when MCD–$UNCD_{Au/Si\text{-}pyramid}$ nanoemitters were used as the cathode, whereas $(J_{pl.})_{UNCD/Au/Si\text{-}pyramid} = 6.20\ mA\ cm^{-2}$ was observed when $UNCD_{Au/Si\text{-}pyramid}$ nanoemitters were used as the cathode.

## Acknowledgements

The authors appreciate the financial support from the National Science Council through the project no. NSC 101-2112-M-032-002 and NSC 101-2221-E-007-064-MY3.

## Notes and references

1 K. H. Becker, K. H. Schoenbach and J. G. Eden, *J. Phys. D: Appl. Phys.*, 2006, **39**, R55.
2 K. H. Schoenbach, R. Verhappen, T. Tessnow, P. F. Peterkin and W. Byszewski, *Appl. Phys. Lett.*, 1996, **68**, 13.
3 J. W. Frame, D. J. Wheeler, T. A. DeTemple and J. G. Eden, *Appl. Phys. Lett.*, 1997, **71**, 1165.
4 S. J. Park and J. G. Eden, *Appl. Phys. Lett.*, 2002, **81**, 4127.
5 C. Penache, M. Miclea, A. Bräuning-Demian, O. Hohn, S. Schössler, T. Jahnke, K. Niemax and H. Schmidt-Böcking, *Plasma Sources Sci. Technol.*, 2002, **11**, 476.
6 S. J. Park, J. Chen, C. J. Wagner, N. P. Ostrom, C. Liu and J. G. Eden, *IEEE J. Sel. Top. Quantum Electron.*, 2002, **8**, 139.
7 S. J. Park, J. G. Eden, J. Chen and C. Liu, *Appl. Phys. Lett.*, 2004, **85**, 4869.
8 S. J. Park, K. F. Chen, N. P. Ostrom and J. G. Eden, *Appl. Phys. Lett.*, 2005, **86**, 111501.
9 K. F. Chen, N. P. Ostrom, S. J. Park and J. G. Eden, *Appl. Phys. Lett.*, 2006, **88**, 061121.
10 S. Mitea, M. Zeleznik, M. D. Bowden, P. W. May, N. A. Fox, J. N. Hart, C. Fowler, R. Stevens and N. StJ. Braithwaite, *Plasma Sources Sci. Technol.*, 2012, **21**, 022001.
11 D. M. Gruen, *Annu. Rev. Mater. Sci.*, 1999, **29**, 211.
12 J. A. Carlisle and O. Auciello, *Electrochem. Soc. Interface*, 2003, 28.
13 K. Chakrabarti, R. Chakrabarrti, K. K. Chattopadhyay, S. Chaudhrui and A. K. Pal, *Diamond Relat. Mater.*, 1998, **7**, 845.
14 V. Ralchenko, A. Karabutov, I. Vlasov, V. Frolov, V. Konov, S. Gordeev, S. Zhukov and A. Dementjev, *Diamond Relat. Mater.*, 1996, **8**, 1496.
15 S. G. Wang, Q. Zhan, S. F. Yoon, J. Ahn, Q. Wang, Q. Zhou and D. J. Yang, *Phys. Status Solidi A*, 2002, **193**, 546.
16 V. Mortet, O. Elmazria, M. Nesladek, M. B. Assouar, G. Vanhoyland, J. D'Haen, M. D. Olieslaeger and P. Alnot, *Appl. Phys. Lett.*, 2002, **81**, 1720.
17 D. Pradhan and I. N. Lin, *ACS Appl. Mater. Interfaces*, 2009, **1**, 1444.
18 J. P. Thomas, H. C. Chen, S. H. Tseng, H. C. Wu, C. Y. Lee, H. F. Cheng, N. H. Tai and I. N. Lin, *ACS Appl. Mater. Interfaces*, 2012, **4**, 5103.
19 J. P. Thomas, H. C. Chen, N. H. Tai and I. N. Lin, *ACS Appl. Mater. Interfaces*, 2011, **3**, 4007.
20 R. H. Fowler and L. Nordheim, *Proc. R. Soc. London, Ser. A*, 1928, **119**, 173.
21 Y. F. Tzeng, Y. C. Lee, C. Y. Lee, I. N. Lin and H. T. Chiu, *Appl. Phys. Lett.*, 2007, **91**, 063117.
22 T. H. Chang, K. Panda, B. K. Panigrahi, S. C. Lou, C. L. Chen, H. C. Chan, I. N. Lin and N. H. Tai, *J. Phys. Chem. C*, 2012, **116**, 19867.
23 J. Michler, Y. Von Kaenel, J. Stiegler and E. Blank, *J. Appl. Phys.*, 1998, **81**, 187.
24 A. C. Ferrari and J. Robertson, *Phys. Rev. B: Condens. Matter Mater. Phys.*, 2000, **61**, 14095.
25 Z. Sun, J. R. Shi, B. K. Tay and S. P. Lau, *Diamond Relat. Mater.*, 2000, **9**, 1979.
26 A. C. Ferrari and J. Robertson, *Phys. Rev. B: Condens. Matter Mater. Phys.*, 2001, **63**, 121405.
27 B. Chapman, *Glow Discharge Processes*, John Wiley & Sons, New York, 1980.
28 I. N. Lin, H. C. Chen, C. S. Wang, Y. R. Lee and C. Y. Lee, *CrystEngComm*, 2011, **13**, 6082.
29 K. J. Sankaran, K. Panda, B. Sundaravel, H. C. Chen, I. N. Lin, C. Y. Lee and N. H. Tai, *ACS Appl. Mater. Interfaces*, 2012, **4**, 4169.